ACS MATERIALS LETTERS

www.acsmaterialsletters.org

Volumetric Additive Manufacturing of Composites via Hydrogel Infusion

Published as part of ACS Materials Letters special issue "Emerging Investigators in Materials Science".

Yiming Ji, Enze Su, and Daryl W. Yee*

Cite This: *ACS Materials Lett.* 2025, 7, 2850–2857

Read Online

ACCESS | Metrics & More | Article Recommendations | Supporting Information

ABSTRACT: Volumetric additive manufacturing (VAM) is an emerging vat photopolymerization technology that boasts improved fabrication speeds, material isotropies, and surface finishes. However, as VAM is only compatible with highly transparent polymer resins, it is extremely challenging to fabricate composites, since it involves the use of resins that contain light-scattering fillers. In this work, we circumvent the transparency criterion by synthesizing the fillers *in situ* post-fabrication, thus enabling the fabrication of composites using VAM. To demonstrate the versatility and utility of our approach, we converted Xolography-printed hydrogels into magnetic and conductive hydrogel composites with filler weight fractions of up to 65 wt %. We further show that filler growth can be spatially controlled, which enables the fabrication of multimaterial structures. This work presents a facile strategy for the VAM of functional composites and multimaterial structures, which could pave the way toward the fabrication of previously impossible devices and smart materials.

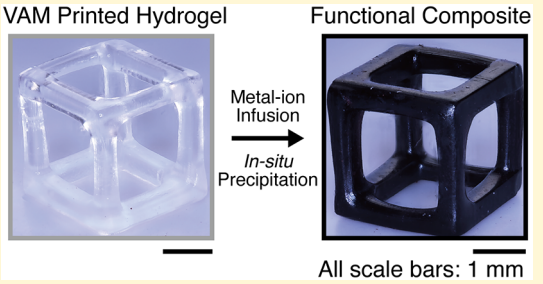

Over the past decades, vat photopolymerization (VP) — a family of additive manufacturing (AM) techniques that utilizes spatial photopolymerization of a liquid resin in a vat to achieve the fabrication of 3D structures[1] — has emerged as an important technology for the fabrication of functional materials and devices.[2−8] VP techniques such as stereolithography and digital light processing printing have gained popularity, as they are inexpensive, offer high print resolutions[9] and print speeds,[10] and are compatible with a variety of materials.[11−15] However, as these technologies utilize a layer-by-layer fabrication approach, they are limited in the range of photoresin viscosities that they can accommodate,[16,17] and the printing speeds,[18] surface finishes,[19,20] and material isotropies[21] that they can achieve.

Volumetric additive manufacturing (VAM), a recently developed VP technology, has the potential to address these limitations.[22,23] Unlike layer-by-layer VP processes, VAM techniques directly polymerize the desired structures within the volume of the vat, using either a tomographic[24−30] or dual-wavelength approach,[31−34] allowing for structures with smoother surfaces and improved material isotropy. From a materials standpoint, VAM enables the use of highly viscous resins[17,35−38] and the fabrication of ultrasoft polymers,[39−42] which significantly expands the range of achievable polymer properties.[43] However, as VAM requires the precise delivery of light throughout the entire vat, it is largely only compatible with highly transparent resins. Consequently, the fabrication of composites with VAM is challenging, as the inclusion of fillers within the resin results in significant light scattering, leading to unsuccessful fabrication.[27,44] Fillers that have a low refractive index mismatch with the resin[45] and/or are much smaller than the wavelength of light[46] can reduce the issue of light scattering during VAM, but they do not fully eliminate the problem, especially at higher filler loadings. More importantly, these mitigation strategies severely limit the range of composite compositions and properties achievable with VAM.

In this study, we report a facile and versatile strategy for the VAM of hydrogel composites with tunable filler weight fractions. Inspired by prior research on the synthesis of biomineralized hydrogels,[47,48] we developed a hydrogel infusion process that enables the *in situ* synthesis of fillers within VAM printed hydrogels, effectively transforming them into composites. Importantly, because these fillers are only introduced post-fabrication, the challenges associated with particle-induced light scattering during printing are completely

Received: February 25, 2025
Revised: July 2, 2025
Accepted: July 3, 2025
Published: July 10, 2025

https://doi.org/10.1021/acsmaterialslett.5c00407
ACS Materials Lett. 2025, 7, 2850−2857

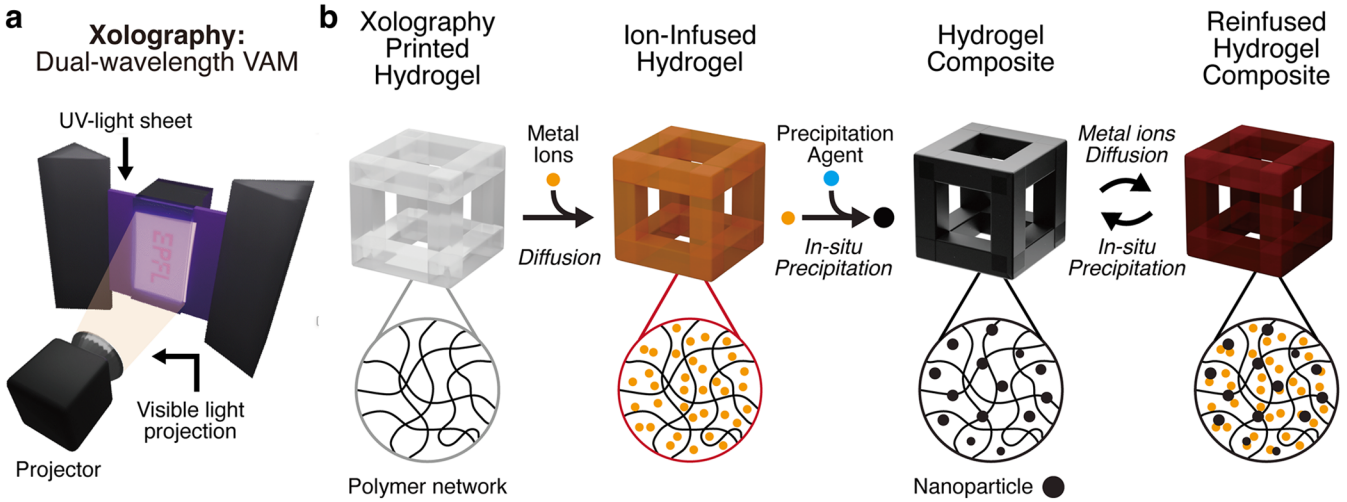

Figure 1. a) Operating principle of Xolography: polymerization occurs only at the intersection of the UV-light sheet and the visible light projection. b) Schematic of the hydrogel-to-composite transformation process. Xolography-fabricated hydrogels are first infused with metal-ion precursors and subsequently infused with precipitating agents to initiate the *in situ* precipitation of nanoparticles within the hydrogel. The infusion-precipitation process can be repeated to tune the volume fraction of the nanoparticles within the composite.

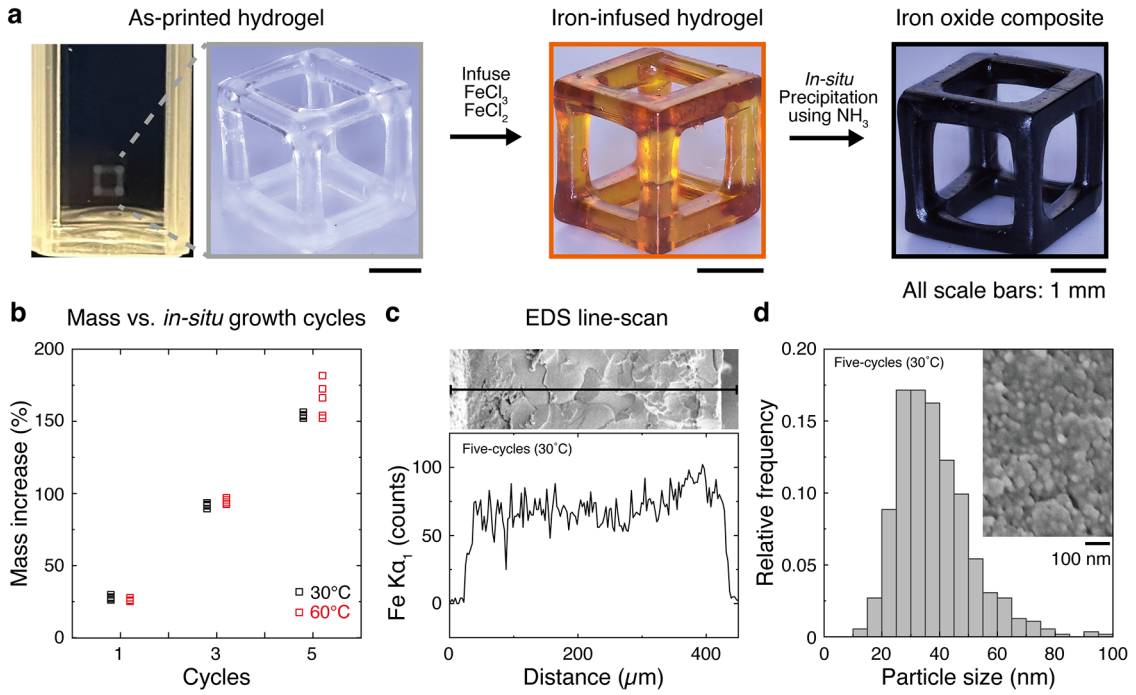

Figure 2. a) Optical images of the "blank" PEGDA-based hydrogel (left: in cuvette and after development), iron-infused hydrogel (middle), and iron oxide nanoparticle (IONP) hydrogel composite (right). b) Mass increase in the hydrogel as a function of the number of IONP synthesis cycles. c) EDS line scan of an IONP composite cross section (five cycles, 30 °C). Iron was detected throughout the cross section of the structure. d) Histogram of IONP sizes measured from SEM images taken from cross sections of an IONP composite (five cycles, 30 °C). The average particle size was 38 ± 13 nm (N = 554).

circumvented, allowing us to utilize routine VAM processes for composite fabrication. To demonstrate the versatility of our approach, we show that hydrogels fabricated using Xolography[31] can be converted into multifunctional composites.

As shown schematically in Figure 1, 3D "blank" hydrogels fabricated with Xolography (Figure 1a) are first soaked in a metal salt solution to infuse them with the desired metal ions. The metal-ion-infused hydrogels are then immersed in a solution containing precipitating agents, which induce the *in situ* precipitation of metal-containing nanoparticles within the hydrogel (Figure 1b). By controlling the infusion-precipitation parameters and the number of infusion-precipitation cycles, the composition and amount of fillers in the composite can be precisely tuned, allowing for tailored material properties. Similar to hydrogel infusion additive manufacturing (HIAM) technology,[49] our composite fabrication process enables a single resin formulation to be used for the fabrication of a variety of composites.

To demonstrate the simplicity and utility of our approach, we first grew magnetic iron oxide nanoparticles (IONPs) within Xolography-printed poly(ethylene glycol) diacrylate (PEGDA)-based hydrogels. Iron oxide was chosen as our

https://doi.org/10.1021/acsmaterialslett.5c00407
ACS Materials Lett. 2025, 7, 2850−2857

model material since a) IONP synthesis is well established,[50] b) magnetic hydrogels can function as remote actuators,[51,52] and c) IONP-polymer composite resins are currently incompatible with VAM due to the significant index of refraction mismatch between IONP and most polymers. The IONP were synthesized *in situ* via the ammonia-induced coprecipitation of Fe^{2+} and Fe^{3+} salts.[53] In brief, the as-printed hydrogels were first immersed in an aqueous solution of $FeCl_2$ and $FeCl_3$, and then in a 30% ammonia solution to transform them into IONP composites (Figure 2a).

Since the mass of iron salts infused into the hydrogel is proportionate to the mass of IONP synthesized *in situ*, we investigated how the infusion conditions impacted the loading of metal salts within the hydrogel. As expected, increasing the concentration of iron salts in the infusion solution led to a proportionate increase in the mass of iron salts within the hydrogel (Figure S1a). Based on these results, a solution of 1.5 M $FeCl_2$ and 2.7 M $FeCl_3$ was chosen due to solubility issues at higher concentrations. Similarly, increasing the infusion temperature and time increased the loading of iron salts in the hydrogel (Figure S1b). However, given the acidic nature of these iron salt solutions, prolonged immersion at high temperatures resulted in surface pitting and damaged the hydrogels, making them difficult to handle. As such, we utilized an infusion temperature and time of 60 °C and 120 min, respectively. At these infusion conditions, we observed a mass increase of 70% while still qualitatively maintaining the integrity of the hydrogel.

We next investigated the relationship between the coprecipitation conditions and the mass of IONPs grown *in situ* (Figure S1c). A mass increase of approximately 25% was observed across all combinations of the tested coprecipitation temperatures (30 °C or 60 °C) and times (5, 10, or 15 min), with no significant differences between them, suggesting that the coprecipitation of IONP was completed within 5 min. Unsurprisingly, we noticed an increase in the extent of surface pitting and the formation of cracks with longer exposure to ammonia (Figure S2a,b), likely due to the base-catalyzed hydrolysis of the acrylic esters in the polymer. Since the coprecipitation temperature would likely affect the crystallinity and properties of the *in situ* synthesized IONPs, we conducted the coprecipitation process at 30 °C or 60 °C for 5 min to assess its impact (*vide infra*).

Unlike conventional composite resins, where the weight fraction of the filler is fixed, our *in situ* synthesis approach allows us to continuously modify the composite composition by repeating the infusion-coprecipitation process (Figure 1b). Using the previously optimized reaction conditions, we observed an approximately linear increase in composite mass with the number of infusion-coprecipitation cycles (Figure 2b). After five growth cycles, composites with 60−65 wt % IONP (depending on the coprecipitation temperature) were obtained. This is notable as the VAM of composites with such high filler fractions of non-index-matched fillers, such as IONP, is often challenging to achieve; Agrawal et al. showed that significant print inaccuracies already occurred when resins with >0.5 wt % of stainless-steel microspheres (1−22 μm) were used.[44] To date, the only way to print with non-index-matched fillers is to use extremely small nanoparticles. Sänger et al. achieved ZrO_2 loadings of 70 wt % by using 5 nm nanoparticles. However, even with such small ZrO_2 particles, the transmittance of their resin at 405 nm was still <60%.[46] It is worth mentioning that even for index-matched fillers, such as SiO_2 (40 nm), only loadings <60 wt % (See SI Discussion 1 for wt % calculations) have been achieved since light scattering becomes a challenge above that.[45,54,55] The high fill fractions of non-index-matched fillers in our composites highlight the utility of our *in situ* synthesis approach.

However, the *in situ* growth of fillers in the hydrogel is also accompanied by an isotropic expansion of the structure. Linear expansions of 5.3 ± 1.1, 15.5 ± 0.4, and 20.6 ± 1.9% were observed after 1, 3, and 5 cycles of IONP growth, respectively (Figure S3). This behavior was expected since the fillers grew within the free volume of the polymer. As the volume fraction of fillers increases, the polymer network expands to accommodate them, leading to a progressively larger increase in the volume of the structure. This linear expansion has to be taken into consideration when fabricating composites with precise dimensions; the VAM-fabricated hydrogel structures need to have slightly smaller dimensions to compensate for the expected expansion during the composite conversion process. Changing the *in situ* synthesis conditions (*vide infra*) and the composition of the polymer will impact the degree of expansion observed, but this is outside the scope of this study (SI Discussion 2).

We further observed that there was a limit to the number of infusion-coprecipitation cycles that could be conducted on our hydrogels; samples subjected to more than five growth cycles at a coprecipitation temperature of 60 °C exhibited noticeable cracking and were fragile. This relationship between the number of growth cycles, reaction temperature, and the extent of damage was expected given the degradation caused by the acid-and base-catalyzed hydrolysis of the polymer and the internal stresses generated during IONP growth. Considering these results, only composites fabricated using one (30 °C and 60 °C), three (30 °C and 60 °C), or five (30 °C) *in situ* growth cycles were investigated further.

To determine the distribution and size of the IONP in the hydrogel composites, we investigated cross sections of dried IONP hydrogel composites using scanning electron microscopy (SEM) and energy dispersive X-ray spectroscopy (EDS). EDS line scans indicated that iron was detected homogeneously throughout the beams, suggesting that the IONPs were distributed well in the composite (Figure 2c). We observed that particle size increased with the number of coprecipitation cycles and with coprecipitation temperature; IONP composites made using three cycles of coprecipitation at 30 and 60 °C had average particle sizes of 10 ± 4 and 17 ± 4 nm, respectively (Figure S4). IONP composites made using five cycles of coprecipitation at 30 °C had average particle sizes of 38 ± 13 nm (Figure 2d). Due to the insulating nature of the polymer matrix, the small size of the IONPs, and the challenges associated with magnetic nanoparticle imaging,[56] we were unable to accurately discern the sizes of the IONPs made with less than three growth cycles.

The magnetic properties of the dried IONP composites were measured by using a vibrating-sample magnetometer (VSM) (Figure 3a). As expected, increasing the mass of IONPs in the composites led to an increase in their magnetic properties. Composites fabricated at higher temperatures had a marked increase in their magnetization despite having a similar amount of IONP in the hydrogel (Figure 2b). For example, three-cycle composites fabricated at 30 and 60 °C exhibited magnetizations of approximately 5 and 15 emu/g, respectively, at 15 kOe. The increase in magnetization was likely due to the slightly improved crystallinity of the IONPs at higher

https://doi.org/10.1021/acsmaterialslett.5c00407
ACS Materials Lett. 2025, 7, 2850−2857

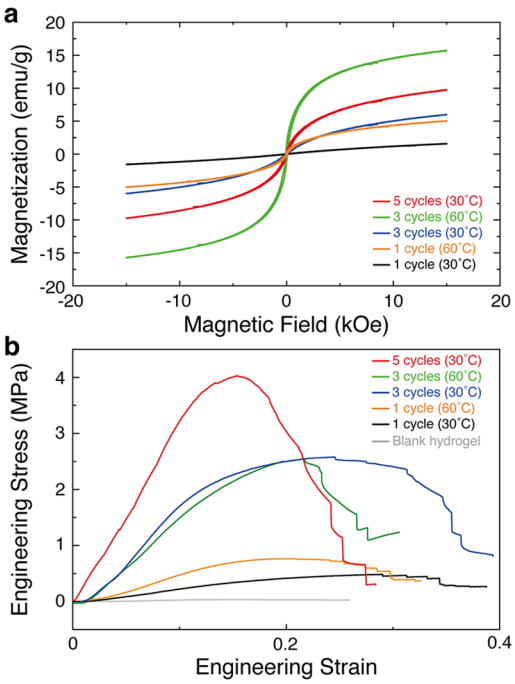

Figure 3. a) Hysteresis loops (measured by VSM, 300 K) and b) representative engineering stress−strain curves (measured in compression) of dried IONP composites fabricated at varying temperatures and number of infusion-coprecipitation cycles.

temperatures (Figure S5). We further observed that coprecipitation temperature, instead of growth rounds, played a much larger role in the composite magnetic properties; 1-cycle composites fabricated at 60 °C had similar magnetic properties as 3-cycle composites fabricated at 30 °C. Considering that the 1-cycle composites exhibited lower linear expansions (~5%) than their 3-cycle counterparts (~15%) (Figure S3), these results suggest that optimizing the reaction conditions to enhance filler properties could be a strategy to mitigate structural expansion.

Given the increased risk of damage to the hydrogel matrix with higher coprecipitation temperatures and growth cycles (Figure S2c-d), we examined the impact of coprecipitation conditions on the compressive mechanical properties of the composites (Figure 3b). Compared to the dried "blank" polymers, all of the dried composites showed a significant increase in their compressive strength, increasing with the number of particle growth cycles. However, the strain at the onset of structural failure increased and then decreased with the number of growth cycles (Figure S6, Table S1). For example, the three-cycle and five-cycle composites fabricated at 30 °C had a maximum compressive stress of 2.52 ± 0.13 and 3.87 ± 0.39 MPa and an onset of structural failure strain of 0.24 ± 0.01 and 0.16 ± 0.01, respectively. For comparison, the "blank" polymer had a maximum compressive stress and onset of structural failure strain of 0.03 ± 0.01 MPa and 0.17 ± 0.02, respectively. We postulate that the increase in failure strain resulted from the softening of the polymer matrix due to the hydrolysis of cross-links during infusion and coprecipitation, which outweighed the stiffening effects of the IONPs. However, as the wt % of IONP increased, the stiffer IONP played a more dominant role in the composite, leading to a decrease in the structural failure strain. Nanoindentation of the dried composites and polymers confirmed that their difference in mechanical properties arose due to the presence of IONP in the composites (Figure S7). The mechanical properties of the IONP composites were observed to be stable over a period of 7 days in water (Figure S8, Table S1, and Supporting Information Discussion 3). Increasing the coprecipitation temperature was observed to be detrimental to the mechanical properties of the composites. Composites fabricated at 60 °C

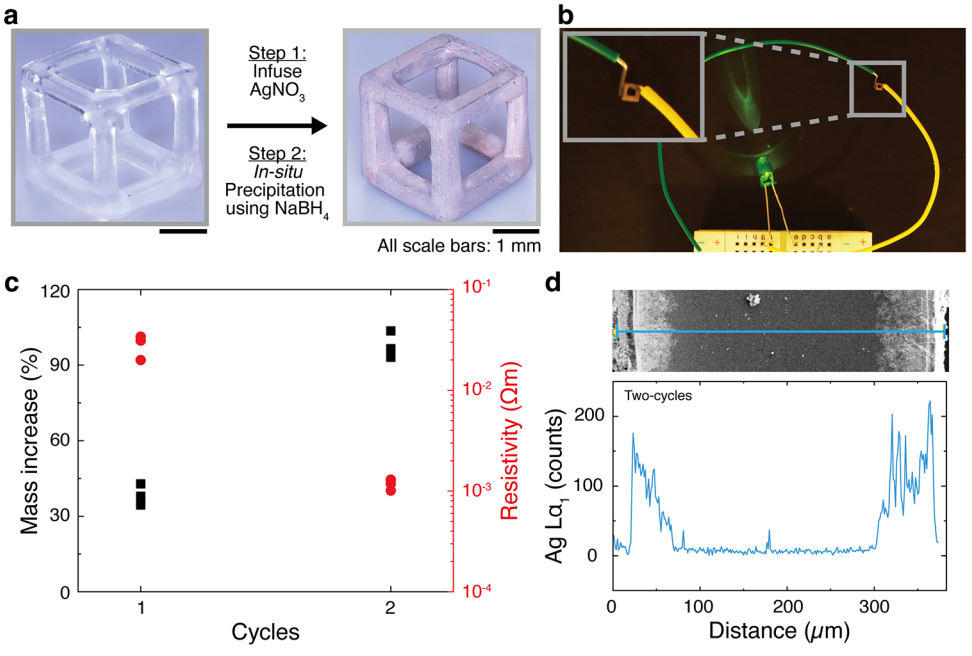

Figure 4. a) Optical images of a "blank" hydrogel (left) and a silver hydrogel composite (right). b) Optical image of a dried silver hydrogel composite (one *in situ* synthesis cycle) closing a light-emitting diode circuit. c) Mass increase (left *y*-axis, black) and resistivity (right *y*-axis, red) of the dried Ag hydrogel composites as a function of the number of *in situ* silver synthesis cycles. d) EDS line scan of an Ag composite cross-section (two cycles). Silver was only detected within 60 μm of the surface.

https://doi.org/10.1021/acsmaterialslett.5c00407
ACS Materials Lett. 2025, 7, 2850−2857

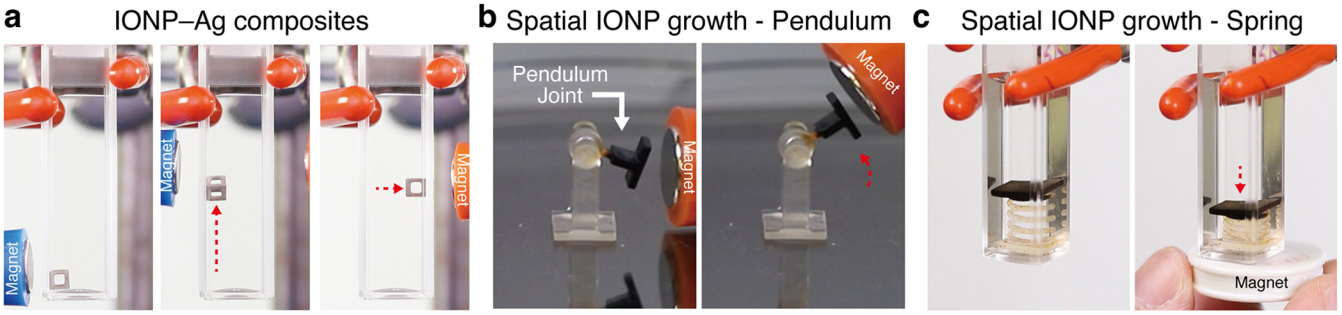

Figure 5. a) Magnetically responsive IONP-Ag hydrogel composites. Magnetic actuation of a multimaterial b) pendulum structure and c) spring fabricated via spatial control of IONP growth.

exhibited a larger variance in their maximum compressive strength, likely due to the increase in defect density (Table S1). Taken together, although higher coprecipitation temperatures improve the magnetic properties of the composite, they appeared to negatively impact its mechanical properties. Nevertheless, the results from our mechanical and magnetic measurements indicate that the composite properties can be precisely tuned with our approach.

Beyond the base-induced coprecipitation of IONP, other nanoparticle synthesis reactions can be utilized to obtain different functional composites. To highlight the versatility of our approach, we fabricated conductive silver hydrogel composites by infusing the "blank" hydrogels with a silver nitrate solution and then reducing the silver ions into silver nanoparticles using sodium borohydride[57] (Figure 4a). The dried Ag composites appeared silver and had a resistivity of approximately 3×10^{-2} Ωm (Figure 4c), which was sufficiently low to close an electrical circuit (Figure 4b). X-ray diffraction (XRD) (Figure S9) confirmed the presence of silver in the composite, validating the success of the *in situ* reduction reaction. The mass of silver in the Ag hydrogel could be increased by repeating the silver infusion-reduction cycle, which resulted in a concomitant decrease in its resistivity (Figure 4c); after two cycles of silver growth, the Ag composites exhibited a resistivity of approximately 1×10^{-3} Ωm. The resistivities of the two-cycle Ag composites remained stable even after exposure to water or air for 7 days (Table S2, Supporting Information Discussion 3). We further observed that there was a limit to the number of *in situ* silver synthesis cycles that could be conducted on the composite structures with significant cracking occurring beyond two cycles of silver growth. We postulate that this was due to the internal stresses generated within the composite from the formation of silver, H_2 gas, and the other byproducts during the sodium borohydride reduction process. Interestingly, EDS line scans of dried Ag composite cross sections revealed a core−shell microstructure, with silver only present within 30 and 60 μm of the surface for the one-cycle and two-cycle composites, respectively (Figure S10 and Figure 4d). The size of the silver nanoparticles in the two-cycle Ag composites, as determined from the SEM images (Figure S10), was approximately 148 ± 78 nm. A possible explanation for the inhomogeneous growth of silver is the rapid kinetics of silver nanoparticle formation as compared to IONP. As sodium borohydride rapidly reduces metal ions, it is possible that it is unable to diffuse far into the volume of the structure, as it is rapidly being consumed by the counter-diffusing silver ions. The mechanism of the Ag shell formation is currently a subject of a future study. These results suggest that core−shell composites can be fabricated with our approach, which is not only impossible with conventional composite resin approaches but could also potentially allow for more efficient placement of functional fillers.

Thus far, we have demonstrated only the repeated *in situ* synthesis of particles with the same composition. However, by changing the composition of the metal salts used during the reinfusion process, composites with multiple fillers can be fabricated. By combining both the IONP and Ag composite synthesis protocols, we fabricated IONP-Ag composites by first conducting three cycles of IONP *in situ* growth, followed by one cycle of Ag growth. The IONP-Ag composites appeared silver but still maintained their magnetic properties, as observed by our ability to manipulate them using an external magnet (Figure 5a, Video S1). Consistent with our previous results, EDS line scans of the dried IONP-Ag composite cross sections revealed a core−shell microstructure, with iron distributed homogeneously throughout the beam and silver only present within 30 μm of the surface (Figure S11). These results highlight our ability to fabricate multifunctional composites using our infusion-precipitation approach.

Finally, our *in situ* synthesis approach also enables the fabrication of multimaterial structures. Since the fillers are only grown under specific reaction conditions, their formation can be spatially controlled by selectively initiating the (co)-precipitation reactions. To demonstrate this, we printed springs and pendulums and selectively grew IONP in the structure to enable remote actuation with an external magnet (Figure 5b-c; Videos S2 and S3). Spatial growth was achieved by precisely infusing selected areas of the structure with the iron-ions before immersing the entire structure into the ammonia solution (see Methods section in the SI).

In both demonstrations, the ability to spatially control the IONP distribution enabled precise actuation of the structures. For example, with the pendulum structure, by growing the IONP only within the pendulum joint, we were able to use an external magnet to rotate that joint without lateral translation of the entire structure (Figure 5b). Similarly, by confining IONP growth to the top plate of the spring, actuation was driven exclusively by the movement of the top plate with no contribution from the rest of the structure (Figure 5c). These examples illustrate how spatial control of filler growth can enable multimaterial fabrication and highlight its potential in enabling previously challenging behaviors. Beyond the IONP-composites and hydrogel multimaterial structures shown here, our approach can be extended to fillers of different compositions and also combined with more precise spatial growth methods, such as light-induced precipitation,[58−60] ion-

https://doi.org/10.1021/acsmaterialslett.5c00407
ACS Materials Lett. 2025, 7, 2850−2857

transfer printing,[61,62] or inkjet printing of the reagents.[63,64] We expect that the development of more precise spatial growth methods will help to reduce polymer degradation during the fabrication process. Currently, our multimaterial fabrication approach exposes the entire structure to ammonia, even in regions that do not contain metal-ions, which could result in unwanted polymer degradation. However, given the mild ammonia reaction conditions (10 min, room temperature, three cycles), no noticeable degradation was observed in the metal-ion free regions of the hydrogel.

In summary, we present a facile method for the VAM of functional hydrogel composites. Unlike current approaches that focus on maximizing resin transparency in composite resins, we circumvent the transparency criterion by synthesizing the functional fillers *in situ* post-VAM. Our approach enables the fabrication of composites with tunable filler weight fractions, reaching up to 65 wt % in our IONP-composites. Additionally, we demonstrate the versatility of our post-fabrication *in situ* synthesis approach; composites with different fillers can be fabricated by modifying the *in situ* synthesis reactions used. Furthermore, by spatially controlling the infusion-precipitation process, we also demonstrate the fabrication of multimaterial structures. Importantly, our work highlights the utility of post-fabrication transformation approaches, where a single resin composition is used to fabricate a variety of different materials. In doing so, we simplify the typically tedious and highly iterative resin design and formulation process associated with VP. Although this work only presents structures fabricated with Xolography, the approach can easily be translated to other VP techniques where transparency is key, such as in multiphoton lithography. It is important to note that a limitation of our current approach is that only a limited number of *in situ* synthesis cycles can be conducted on the polymer due to degradation during the infusion and coprecipitation process. This limits the mass of functional fillers that can be grown and, by extension, the properties of the composites. Moving forward, we expect that the use of polymers that are more resistant to hydrolysis compared with polyacrylates, such as polyamides, will mitigate polymer degradation and enable higher filler loadings. In addition, these polymers could increase the long-term stability and durability of the composites in acidic and basic environments, which would expand their application window. Nevertheless, the demonstrated capability to fabricate composites with VAM technology is a significant advancement in the state of the art and could enable the fabrication of previously inaccessible functional materials and devices. We anticipate that our findings will have a direct implication in fields where composite materials are necessary, from biomedical devices to sensors.

■ ASSOCIATED CONTENT

Supporting Information

The Supporting Information is available free of charge at https://pubs.acs.org/doi/10.1021/acsmaterialslett.5c00407.

Supporting Information: Materials and experimental methods; characterization of materials; CAD drawings of the printed structures; additional discussions on SiO_2 calculations, mitigating structural expansion, composite stability, and nanoparticle surface functionalization (PDF)

Video S1: Magnetic control of IONP-Ag composites (MP4)

Video S2: Magnetic actuation of multimaterial IONP pendulum (MP4)

Video S3: Magnetic actuation of multimaterial IONP spring (MP4)

■ AUTHOR INFORMATION

Corresponding Author

Daryl W. Yee − *Institute of Electrical and Micro Engineering, École Polytechnique Fédérale de Lausanne (EPFL), Lausanne CH-1015, Switzerland;* orcid.org/0000-0002-4114-6167; Email: daryl.yee@epfl.ch

Authors

Yiming Ji − *Institute of Electrical and Micro Engineering, École Polytechnique Fédérale de Lausanne (EPFL), Lausanne CH-1015, Switzerland;* orcid.org/0000-0003-0891-6462

Enze Su − *Applied Materials Science, Department of Materials Science and Engineering, Uppsala University, Uppsala SE-751 05, Sweden*

Complete contact information is available at: https://pubs.acs.org/10.1021/acsmaterialslett.5c00407

Author Contributions

Y.J., E.S., and D.W.Y. conceived and designed the experiments. E.S. optimized the printing procedure. E.S. and Y.J. developed and optimized the infusion-coprecipitation process. Y.J. performed all the materials characterizations. E.S. fabricated the multimaterial structures. The manuscript was written through contributions of all authors. All authors have given approval to the final version of the manuscript. CRediT: **Yiming Ji** conceptualization, data curation, formal analysis, investigation, methodology, supervision, visualization, writing - original draft, writing - review & editing; **Enze Su** conceptualization, data curation, formal analysis, investigation, methodology, validation, visualization, writing - original draft, writing - review & editing; **Daryl W Yee** conceptualization, formal analysis, funding acquisition, investigation, methodology, project administration, resources, supervision, validation, visualization, writing - original draft, writing - review & editing.

Funding

This work was partially supported by the Swiss ETH domain Strategic Focus Area − Advanced Manufacturing program.

Notes

A preprint of this paper is available on ChemRxiv.[65]

The authors declare the following competing financial interest(s): A patent has been filed on this work.

■ ACKNOWLEDGMENTS

The authors would like to acknowledge the following people and organizations: Dr. Niklas König from xolo GmbH for assistance with resin formulation and print optimization. xolo GmbH for the loan of a Xube system and for providing the hydrogel resins and the dual-color photoinitiators. Miguel Ángel Herrero Vañó and Dr. Renato Pero from Alemnis AG (Thun, Switzerland) for support with nanoindentation investigations. Dr. Pascal Schouwink for assistance with nanoparticle characterization. Yichi Luo for assistance with optical characterization of the multimaterial structures. Terence Ho for assistance with mechanical testing of the

composites. D.W.Y. acknowledges the financial support from the Swiss ETH domain Strategic Focus Area – Advanced Manufacturing program.

REFERENCES

(1) F42 Committee. Terminology for Additive Manufacturing - General Principles - Terminology. DOI: 10.1520/F3177-21.
(2) Van Der Linden, P. J. E. M.; Popov, A. M.; Pontoni, D. Accurate and Rapid 3D Printing of Microfluidic Devices Using Wavelength Selection on a DLP Printer. *Lab. Chip* **2020**, *20*, 4128–4140.
(3) Huang, C.; Wen, S.; Hsiao, C.; Zhang, C.; Lin, K.; Yu, S. Digital Light Processing of Soft Robotic Gripper with High Toughness and Self-Healing Capability Achieved by Deep Eutectic Solvents. *Adv. Funct. Mater.* **2024**, *34*, No. 2314101.
(4) Yee, D. W.; Hetts, S. W.; Greer, J. R. 3D-Printed Drug Capture Materials Based on Genomic DNA Coatings. *ACS Appl. Mater. Interfaces* **2021**, *13*, 41424–41434.
(5) Huang, P.; Fu, H.; Tan, M. W. M.; Jiang, Y.; Lee, P. S. Digital Light Processing 3D-Printed Multilayer Dielectric Elastomer Actuator for Vibrotactile Device. *Adv. Mater. Technol.* **2024**, *9*, No. 2301642.
(6) Wang, Z.; Hensleigh, R.; Xu, Z.; Wang, J.; Park, J. J.; Papathanasopoulos, A.; Rahmat-Samii, Y.; Zheng, X. R. Ultra-Light Antennas via Charge Programmed Deposition Additive Manufacturing. *Nat. Commun.* **2025**, *16*, 427.
(7) Bertoncini, A.; Liberale, C. 3D Printed Waveguides Based on Photonic Crystal Fiber Designs for Complex Fiber-End Photonic Devices. *Optica* **2020**, *7*, 1487.
(8) Caudill, C.; Perry, J. L.; Iliadis, K.; Tessema, A. T.; Lee, B. J.; Mecham, B. S.; Tian, S.; DeSimone, J. M. Transdermal Vaccination via 3D-Printed Microneedles Induces Potent Humoral and Cellular Immunity. *Proc. Natl. Acad. Sci. U. S. A.* **2021**, *118*, No. e2102595118.
(9) Shafique, H.; Karamzadeh, V.; Kim, G.; Shen, M. L.; Morocz, Y.; Sohrabi-Kashani, A.; Juncker, D. High-Resolution Low-Cost LCD 3D Printing for Microfluidics and Organ-on-a-Chip Devices. *Lab. Chip* **2024**, *24*, 2774–2790.
(10) Zhang, F.; Zhu, L.; Li, Z.; Wang, S.; Shi, J.; Tang, W.; Li, N.; Yang, J. The Recent Development of Vat Photopolymerization: A Review. *Addit. Manuf.* **2021**, *48*, No. 102423.
(11) Yee, D. W.; Greer, J. R. Three-dimensional Chemical Reactors: *In Situ* Materials Synthesis to Advance Vat Photopolymerization. *Polym. Int.* **2021**, *70*, 964–976.
(12) Al Rashid, A.; Ahmed, W.; Khalid, M. Y.; Koç, M. Vat Photopolymerization of Polymers and Polymer Composites: Processes and Applications. *Addit. Manuf.* **2021**, *47*, No. 102279.
(13) Mamatha, S.; Biswas, P.; Johnson, R. Digital Light Processing of Ceramics: An Overview on Process, Materials and Challenges. *Prog. Addit. Manuf.* **2023**, *8*, 1083–1102.
(14) Melentiev, R.; Harakály, G.; Stögerer, J.; Mitteramskogler, G.; Wagih, A.; Lubineau, G.; Grande, C. A. High-Resolution Metal 3D Printing via Digital Light Processing. *Addit. Manuf.* **2024**, *85*, No. 104156.
(15) Li, Y.; Li, C.; Zhang, X.; Wang, Y.; Tan, Y.; Chang, S.; Chen, Z.; Fu, G.; Kou, Z.; Stefan, A.; Xu, X.; Ding, J. Incorporating Metal Precursors towards a Library of High-Resolution Metal Parts by Stereolithography. *Appl. Mater. Today* **2022**, *29*, No. 101553.
(16) Le Fer, G.; Luo, Y.; Becker, M. L. Poly(Propylene Fumarate) Stars, Using Architecture to Reduce the Viscosity of 3D Printable Resins. *Polym. Chem.* **2019**, *10*, 4655–4664.
(17) Bao, Y.; Paunović, N.; Leroux, J. Challenges and Opportunities in 3D Printing of Biodegradable Medical Devices by Emerging Photopolymerization Techniques. *Adv. Funct. Mater.* **2022**, *32*, No. 2109864.
(18) Paral, S. K.; Lin, D.-Z.; Cheng, Y.-L.; Lin, S.-C.; Jeng, J.-Y. A Review of Critical Issues in High-Speed Vat Photopolymerization. *Polymers* **2023**, *15*, 2716.
(19) Kowsari, K.; Zhang, B.; Panjwani, S.; Chen, Z.; Hingorani, H.; Akbari, S.; Fang, N. X.; Ge, Q. Photopolymer Formulation to Minimize Feature Size, Surface Roughness, and Stair-Stepping in Digital Light Processing-Based Three-Dimensional Printing. *Addit. Manuf.* **2018**, *24*, 627–638.
(20) Shan, Y.; Krishnakumar, A.; Qin, Z.; Mao, H. Reducing Lateral Stair-Stepping Defects in Liquid Crystal Display-Based Vat Photopolymerization by Defocusing the Image Pattern. *Addit. Manuf.* **2022**, *52*, No. 102653.
(21) Torres-Alvarez, D.; Celis-Guzman, A.; Aguirre-Soto, A. Resin-Dependent Mechanical Anisotropy in Laser Vat Photopolymerization Correlates to the Initial Rate of Polymerization and Critical Energy. *Addit. Manuf. Lett.* **2025**, *12*, No. 100264.
(22) Thijssen, Q.; Toombs, J.; Li, C. C.; Taylor, H.; Van Vlierberghe, S. From Pixels to Voxels: A Mechanistic Perspective on Volumetric 3D-Printing. *Prog. Polym. Sci.* **2023**, *147*, No. 101755.
(23) Chansoria, P.; Rizzo, R.; Rütsche, D.; Liu, H.; Delrot, P.; Zenobi-Wong, M. Light from Afield: Fast, High-Resolution, and Layer-Free Deep Vat 3D Printing: Focus Review. *Chem. Rev.* **2024**, *124*, 8787–8822.
(24) Kelly, B. E.; Bhattacharya, I.; Heidari, H.; Shusteff, M.; Spadaccini, C. M.; Taylor, H. K. Volumetric Additive Manufacturing via Tomographic Reconstruction. *Science* **2019**, *363*, 1075–1079.
(25) Loterie, D.; Delrot, P.; Moser, C. High-Resolution Tomographic Volumetric Additive Manufacturing. *Nat. Commun.* **2020**, *11*, 852.
(26) Bernal, P. N.; Delrot, P.; Loterie, D.; Li, Y.; Malda, J.; Moser, C.; Levato, R. Volumetric Bioprinting of Complex Living-Tissue Constructs within Seconds. *Adv. Mater.* **2019**, *31*, No. 1904209.
(27) Madrid-Wolff, J.; Boniface, A.; Loterie, D.; Delrot, P.; Moser, C. Controlling Light in Scattering Materials for Volumetric Additive Manufacturing. *Adv. Sci.* **2022**, *9*, No. 2105144.
(28) Waddell, T.; Toombs, J.; Reilly, A.; Schwab, T.; Castaneda, C.; Shan, I.; Lewis, T.; Mohnot, P.; Potter, D.; Taylor, H. Use of Volumetric Additive Manufacturing as an In-Space Manufacturing Technology. *Acta Astronaut* **2023**, *211*, 474–482.
(29) Wang, B.; Engay, E.; Stubbe, P. R.; Moghaddam, S. Z.; Thormann, E.; Almdal, K.; Islam, A.; Yang, Y. Stiffness Control in Dual Color Tomographic Volumetric 3D Printing. *Nat. Commun.* **2022**, *13*, 367.
(30) Álvarez-Castaño, M. I.; Madsen, A. G.; Madrid-Wolff, J.; Sgarminato, V.; Boniface, A.; Glückstad, J.; Moser, C. Holographic Tomographic Volumetric Additive Manufacturing. *Nat. Commun.* **2025**, *16*, 1551.
(31) Regehly, M.; Garmshausen, Y.; Reuter, M.; König, N. F.; Israel, E.; Kelly, D. P.; Chou, C.-Y.; Koch, K.; Asfari, B.; Hecht, S. Xolography for Linear Volumetric 3D Printing. *Nature* **2020**, *588*, 620–624.
(32) Stüwe, L.; Geiger, M.; Röllgen, F.; Heinze, T.; Reuter, M.; Wessling, M.; Hecht, S.; Linkhorst, J. Continuous Volumetric 3D Printing: Xolography in Flow. *Adv. Mater.* **2024**, *36*, No. 2306716.
(33) Stoecker, L.; Cedillo-Servin, G.; König, N. F.; De Graaf, F. V.; García-Jiménez, M.; Hofmann, S.; Ito, K.; Wentzel, A. S.; Castilho, M. Xolography for Biomedical Applications: Dual-Color Light-Sheet Printing of Hydrogels With Local Control Over Shape and Stiffness. *Adv. Mater.* **2025**, *37*, No. 2410292.
(34) Huang, K.; Franchin, G.; Colombo, P. Volumetric Additive Manufacturing of SiOC by Xolography. *Small* **2024**, *20*, No. 2402356.
(35) Peng, S.; Chen, G.; Luo, X.; Zhang, X.; Li, D.; Xu, Y.; Sun, C.; Shang, E.; Wang, X.; Liu, Y. Volumetric 3D Printing of Ionic Conductive Elastomers for Multifunctional Flexible Electronics. *Addit. Manuf.* **2024**, *95*, No. 104536.
(36) Tisato, S.; Vera, G.; Mani, A.; Chase, T.; Helmer, D. An Easy-to-Build, Accessible Volumetric 3D Printer Based on a Liquid Crystal Display for Rapid Resin Development. *Addit. Manuf.* **2024**, *87*, No. 104232.
(37) Corrigan, N.; Li, X.; Zhang, J.; Boyer, C. Xolography for the Production of Polymeric Multimaterials. *Adv. Mater. Technol.* **2024**, *9*, No. 2400162.
(38) König, N. F.; Reuter, M.; Reuß, M.; Kromer, C. S. F.; Herder, M.; Garmshausen, Y.; Asfari, B.; Israel, E.; Vasconcelos Lima, L.; Puvati, N.; Leonhard, J.; Madalo, L.; Heuschkel, S.; Engelhard, M.;

Arzhangnia, Y.; Radzinski, D. Xolography for 3D Printing in Microgravity. *Adv. Mater.* **2025**, *37*, No. 2413391.
(39) Xie, M.; Lian, L.; Mu, X.; Luo, Z.; Garciamendez-Mijares, C. E.; Zhang, Z.; López, A.; Manríquez, J.; Kuang, X.; Wu, J.; Sahoo, J. K.; González, F. Z.; Li, G.; Tang, G.; Maharjan, S.; Guo, J.; Kaplan, D. L.; Zhang, Y. S. Volumetric Additive Manufacturing of Pristine Silk-Based (Bio)Inks. *Nat. Commun.* **2023**, *14*, 210.
(40) Qiu, W.; Gehlen, J.; Bernero, M.; Gehre, C.; Schädli, G. N.; Müller, R.; Qin, X. A Synthetic Dynamic Polyvinyl Alcohol Photoresin for Fast Volumetric Bioprinting of Functional Ultrasoft Hydrogel Constructs. *Adv. Funct. Mater.* **2023**, *33*, No. 2214393.
(41) Bernal, P. N.; Bouwmeester, M.; Madrid-Wolff, J.; Falandt, M.; Florczak, S.; Rodriguez, N. G.; Li, Y.; Größbacher, G.; Samsom, R.; Van Wolferen, M.; Van Der Laan, L. J. W.; Delrot, P.; Loterie, D.; Malda, J.; Moser, C.; Spee, B.; Levato, R. Volumetric Bioprinting of Organoids and Optically Tuned Hydrogels to Build Liver-Like Metabolic Biofactories. *Adv. Mater.* **2022**, *34*, No. 2110054.
(42) Lian, L.; Xie, M.; Luo, Z.; Zhang, Z.; Maharjan, S.; Mu, X.; Garciamendez-Mijares, C. E.; Kuang, X.; Sahoo, J. K.; Tang, G.; Li, G.; Wang, D.; Guo, J.; González, F. Z.; Abril Manjarrez Rivera, V.; Cai, L.; Mei, X.; Kaplan, D. L.; Zhang, Y. S. Rapid Volumetric Bioprinting of Decellularized Extracellular Matrix Bioinks. *Adv. Mater.* **2024**, *36*, No. 2304846.
(43) Madrid-Wolff, J.; Toombs, J.; Rizzo, R.; Bernal, P. N.; Porcincula, D.; Walton, R.; Wang, B.; Kotz-Helmer, F.; Yang, Y.; Kaplan, D.; Zhang, Y. S.; Zenobi-Wong, M.; McLeod, R. R.; Rapp, B.; Schwartz, J.; Shusteff, M.; Talyor, H.; Levato, R.; Moser, C. A Review of Materials Used in Tomographic Volumetric Additive Manufacturing. *MRS Commun.* **2023**, *13*, 764−785.
(44) Agrawal, P.; Zhuang, S.; Dreher, S.; Mitter, S.; Ahmed, D. SonoPrint: Acoustically Assisted Volumetric 3D Printing for Composites. *Adv. Mater.* **2024**, No. 2408374.
(45) Barbera, L.; Madrid-Wolff, J.; Emma, R.; Masania, K.; Boniface, A.; Loterie, D.; Delrot, P.; Moser, C.; Studart, A. R. Multimaterial Volumetric Printing of Silica-Based Glasses. *Adv. Mater. Technol.* **2024**, *9*, No. 2202117.
(46) Sänger, J. C.; König, N. F.; De Marzi, A.; Zocca, A.; Franchin, G.; Bermejo, R.; Colombo, P.; Günster, J. Linear Volumetric Additive Manufacturing of Zirconia from a Transparent Photopolymerizable Ceramic Slurry via Xolography. *Open Ceram.* **2024**, *19*, No. 100655.
(47) Lv, Y.; Wang, Y.; Zhang, X. Construction of Mineralization Nanostructures in Polymers for Mechanical Enhancement and Functionalization. *Small* **2024**, *20*, No. 2309313.
(48) Mao, L.-B.; Meng, Y.-F.; Meng, X.-S.; Yang, B.; Yang, Y.-L.; Lu, Y.-J.; Yang, Z.-Y.; Shang, L.-M.; Yu, S.-H. Matrix-Directed Mineralization for Bulk Structural Materials. *J. Am. Chem. Soc.* **2022**, *144*, 18175−18194.
(49) Saccone, M. A.; Gallivan, R. A.; Narita, K.; Yee, D. W.; Greer, J. R. Additive Manufacturing of Micro-Architected Metals via Hydrogel Infusion. *Nature* **2022**, *612*, 685−690.
(50) Laurent, S.; Forge, D.; Port, M.; Roch, A.; Robic, C.; Vander Elst, L.; Muller, R. N. Magnetic Iron Oxide Nanoparticles: Synthesis, Stabilization, Vectorization, Physicochemical Characterizations, and Biological Applications. *Chem. Rev.* **2008**, *108*, 2064−2110.
(51) Xiong, J.; Zhang, J.; Zhong, Y.; Song, X.; Wang, H.; Cheang, U. K. Magnetically-Actuated Hydrogel-Based Achiral Planar Microswimmers for SERS Detection: In Situ Coprecipitation for Continuous Loading of Iron Oxide Nanoparticles. *Front. Bioeng. Biotechnol.* **2023**, *11*, No. 1086106.
(52) He, Y.; Tang, J.; Hu, Y.; Yang, S.; Xu, F.; Zrínyi, M.; Mei Chen, Y. Magnetic Hydrogel-Based Flexible Actuators: A Comprehensive Review on Design, Properties, and Applications. *Chem. Eng. J.* **2023**, *462*, No. 142193.
(53) Suh, S. K.; Yuet, K.; Hwang, D. K.; Bong, K. W.; Doyle, P. S.; Hatton, T. A. Synthesis of Nonspherical Superparamagnetic Particles: *In Situ* Coprecipitation of Magnetic Nanoparticles in Microgels Prepared by Stop-Flow Lithography. *J. Am. Chem. Soc.* **2012**, *134*, 7337−7343.
(54) Toombs, J. T.; Luitz, M.; Cook, C. C.; Jenne, S.; Li, C. C.; Rapp, B. E.; Kotz-Helmer, F.; Taylor, H. K. Volumetric Additive Manufacturing of Silica Glass with Microscale Computed Axial Lithography. *Science* **2022**, *376*, 308−312.
(55) Myers, L. A.; Schwartz, J. J.; De Beer, M. P.; Walton, R. L.; Porcincula, D. H. Development of Transparent, Particle-loaded Photoresins for Volumetric Additive Manufacturing of Silica Glass. *J. Polym. Sci.* **2024**, *62*, 2683−2691.
(56) Bian, L.; Cao, Q.; Zheng, L.; Liu, Y. Ultramicrotomy Preparation of Magnetic Nanoparticles for Transmission Electron Microscopy. *Ultramicroscopy* **2021**, *227*, No. 113275.
(57) Song, K. C.; Lee, S. M.; Park, T. S.; Lee, B. S. Preparation of Colloidal Silver Nanoparticles by Chemical Reduction Method. *Korean J. Chem. Eng.* **2009**, *26*, 153−155.
(58) Huynh, T.-P.; Pedersen, C.; Wittig, N. K.; Birkedal, H. Precipitation of Inorganic Phases through a Photoinduced pH Jump: From Vaterite Spheroids and Shells to ZnO Flakes and Hexagonal Plates. *Cryst. Growth Des.* **2018**, *18*, 1951−1955.
(59) Bistervels, M. H.; Kamp, M.; Schoenmaker, H.; Brouwer, A. M.; Noorduin, W. L. Light-Controlled Nucleation and Shaping of Self-Assembling Nanocomposites. *Adv. Mater.* **2022**, *34*, No. 2107843.
(60) Mondal, T.; Patra, S.; Mondal, B.; Ghosh, P.; Hamley, I. W.; Banerjee, A. Silver-Containing Metallo Hydrogel as a Nanocatalyst for Hydrogen Evolution. *ACS Appl. Polym. Mater.* **2024**, *6*, No. 11383.
(61) Tang, J.; Zeng, L.; Liu, Z. Fabrication of Patterned Magnetic Hydrogels by Ion Transfer Printing. *Soft Matter* **2021**, *17*, 8059−8067.
(62) Peng, X.; Li, Y.; Zhang, Q.; Shang, C.; Bai, Q.; Wang, H. Tough Hydrogels with Programmable and Complex Shape Deformations by Ion Dip-Dyeing and Transfer Printing. *Adv. Funct. Mater.* **2016**, *26*, 4491−4500.
(63) Wan, X.; Miao, X.; Yao, J.; Wang, S.; Shao, F.; Xiao, S.; Zhan, R.; Chen, K.; Zeng, X.; Gu, X.; Xu, J. In Situ Ultrafast and Patterned Growth of Transition Metal Dichalcogenides from Inkjet-Printed Aqueous Precursors. *Adv. Mater.* **2021**, *33*, No. 2100260.
(64) Zub, K.; Hoeppener, S.; Schubert, U. S. Inkjet Printing and 3D Printing Strategies for Biosensing, Analytical, and Diagnostic Applications. *Adv. Mater.* **2022**, *34*, No. 2105015.
(65) Ji, Y.; Su, E.; Yee, D. W. Volumetric Additive Manufacturing of Composites via Hydrogel Infusion. **2025**, *ChemRxiv*. 10.26434/chemrxiv-2025-1twqq (accessed July 1, 2025).

https://doi.org/10.1021/acsmaterialslett.5c00407
ACS Materials Lett. 2025, 7, 2850−2857